High resolution laser spectroscopy of the $\tilde{C}\,^2\Delta$–$\tilde{X}\,^2\Sigma^+$ transition of CaOH and CaOD: Vibronic coupling and the Renner–Teller effect

C. N. Jarman and P. F. Bernath[a),b)]
Department of Chemistry, University of Arizona, Tucson, Arizona 85721

(Received 25 March 1992; accepted 23 April 1992)

The $\tilde{C}\,^2\Delta$–$\tilde{X}\,^2\Sigma^+$ transition of CaOH and CaOD has been observed in the blue region of the spectrum. This electronically forbidden transition becomes allowed through vibronic coupling with the bending mode. The (010)–(000) band for CaOH and the (010)–(000), (020)–(010), (010)–(010), (000)–(010), and (010)–(02^00) bands for CaOD have been recorded and analyzed at high resolution. The $\tilde{C}\,^2\Delta(000)$ state of CaOD has a band origin at 21 907.128(1) cm^{-1}, a rotational constant B of 0.293 536(7) cm^{-1}, and a spin–orbit constant A of 11.4944(5) cm^{-1}. A rotational analysis of the $\tilde{C}\,^2\Delta(020)\mu\Sigma$ and the $\tilde{C}\,^2\Delta(020)\kappa\Sigma$ states of CaOD has also led to the first experimental determination of the Renner–Teller parameter $\hat{g}_4$ for a $^2\Delta$ state at $\hat{g}_4 = -0.038\,62(9)$ cm^{-1}.

INTRODUCTION

There has been much recent spectroscopic work on molecules consisting of an alkaline earth metal, M, and a univalent ligand, X, with a positive electron affinity (see Refs. 1 and 2 as well as references cited therein). These free radicals possess an electronic structure approximately described as closed shell M^{2+} and X^- ions with a single electron localized in a molecular orbital near the M atom. The properties of their low-lying electronic states are thus determined by the molecular orbital in which the single electron resides. For purely ionic bonding, this molecular orbital can be thought of as arising from atomic orbitals of M^+ perturbed by the negative point charge of a polarizable ligand X^-. This approach was taken by Rice, Martin, and Field[3] who calculated the electronic structure of calcium monohalides. These workers concluded for CaF that the ground state, $X\,^2\Sigma^+$ was predominantly $4s\sigma$, the $A\,^2\Pi$ state $4p\pi$, the $B\,^2\Sigma^+$ state was an equal mixture of $4p\sigma$ and $3d\sigma$, and the $C\,^2\Pi$ state was mainly $5p\pi$ in character. All of these states have been classified in the spectroscopic investigation by Bernath.[4]

Törring, Ernst, and Kändler[1] have also performed calculations on the electronic structure of calcium, strontium, and barium monohalides using a modified Rittner[5] model. Their calculations give better agreement with the experimental data on calcium monohalides than the simple ligand field approach, partly because the model necessitates determining some empirical ion polarizability parameters from the experimental data. The predictions of the modified Rittner model agree well with the experimental data for calcium, strontium, and barium monohalides. More recently still, Ortiz has performed some electron propagator calculations and determined the electronic origins for the ground and excited states of $CaCH_3$, $CaNH_2$, CaOH, and CaF.[6]

One low-lying state in CaF that has eluded experimental detection until recently is the $B'\,^2\Delta$ state, predicted by Rice *et al.*[3] to have an energy $T_0 = 24\,950$ cm^{-1} and a molecular spin–orbit one-electron parameter $a_\delta = 2A = 27$ cm^{-1}, very close to the free ion value $\zeta(Ca^+, 3d) = 24$ cm^{-1}. Other predictions for the energy of this state are 24 415 cm^{-1} by Ortiz,[6] 17 690 cm^{-1} by Törring *et al.*,[1] and 24 851 cm^{-1} by Bündgen *et al.*[7] Electric dipole transitions to this state from the ground state contravene the $\Delta\Lambda = 0, \pm 1$ selection rules, and so are forbidden. The $B'\,^2\Delta_{3/2}$ spin component, however, has recently been observed in fluorescence from the $C\,^2\Pi_{1/2}$ spin component by d'Incan *et al.*,[8] and they determined $T_0 = 21\,530.8$ cm^{-1}, and $B_0^{\text{eff}} = 0.3236(1)$ cm^{-1}, placing the $B'\,^2\Delta$ state at 21 558 cm^{-1}. This observation prompted us to search for the analogous $\tilde{C}\,^2\Delta$ state in CaOH.

Detailed *ab initio* calculations have been performed on CaOH to predict its geometry and dissociation energy[9,10] and its dipole moment.[11] Mestdagh and Visticot have recently extended the modified Rittner method[1] to predict the binding energies and dipole moments of the low-lying electronic states of the alkali (Li to Cs) and alkaline earth (Mg to Ba) monohydroxides.[12] These authors predicted the energy of the $\tilde{C}\,^2\Delta$ state to be 18 362 cm^{-1}, rather far from the 24 366 cm^{-1} value predicted in the electron propagator calculation of Ortiz.[6] It is predicted (and observed for CaF) that the $^2\Delta$ state lies above the $B\,^2\Sigma^+$ state for calcium and strontium derivatives. However, for barium derivatives the $A'\,^2\Delta$ lies below the $A\,^2\Pi$ state with the $B\,^2\Sigma^+$, $A\,^2\Pi$, and $A'\,^2\Delta$ states having the energy ordering appropriate for a d complex. The $A'\,^2\Delta$ state has been found for BaH,[13,14] BaF,[15,16] BaCl,[17,18] and BaOH.[19]

Previous high resolution laser induced fluorescence studies of CaOH and CaOD have enabled spectroscopic constants to be determined for the $\tilde{X}\,^2\Sigma^+$, $\tilde{A}\,^2\Pi$, and $\tilde{B}\,^2\Sigma^+$ states.[20–24] Lately, there has been an increase in the amount of spectroscopic work on this molecule. Coxon, Li, and Presunka have just investigated the excited vibrational levels in the $\tilde{X}\,^2\Sigma^+$ state of CaOH and CaOD by resolved fluorescence spectroscopy,[25] and promise a more extensive investigation of the vibrational structure. The permanent

[a)] Camille and Henry Dreyfus Teacher–Scholar.
[b)] Also: Department of Chemistry, University of Waterloo, Waterloo, Ontario, Canada N2L 3G1.

 0021-9606/92/151711-08$006.00 © 1992 American Institute of Physics

electric dipole moment of CaOH in the $\tilde{X}\,^2\Sigma^+$, $\tilde{A}\,^2\Pi$, and $\tilde{B}\,^2\Sigma^+$ states has been measured very recently by Steimle *et al.*,[26] as has the millimeter wave spectrum of CaOH by Ziurys, Barclay, and Anderson,[27] yielding very accurate spectroscopic constants for the $\tilde{X}\,^2\Sigma^+$ state.

It was hoped that vibronic coupling with the Ca–O–H bending mode by the Herzberg–Teller effect[28] would enable us to record laser excitation spectra to the $\tilde{C}\,^2\Delta$ state from the ground $\tilde{X}\,^2\Sigma^+$ state. Electric-dipole transitions from the $\tilde{X}\,^2\Sigma^+$ to the $\tilde{C}\,^2\Delta$ state are not allowed for CaF because they involve a change in Λ of 2. However, for CaOH, the vibrational angular momentum l associated with the ν_2 Ca–O–H bend couples to the electronic angular momentum Λ of both the $\tilde{C}\,^2\Delta$ and the $\tilde{X}\,^2\Sigma^+$ states to yield a resultant angular momentum $K=\Lambda+l$. Allowed electric-dipole transitions for CaOH now obey $\Delta K=0,\pm1$ instead of the more restrictive $\Delta\Lambda=0,\pm1$ for CaF. For the $\tilde{C}\,^2\Delta$–$\tilde{X}\,^2\Sigma^+$ electronic transition of CaOH, this means that transitions with $\Delta v_2 = \pm1, \pm3, \cdots$ obey $\Delta K\pm1$, and transitions with $\Delta v_2 = 0, \pm2, \cdots$ obey $\Delta K=0$. As usual for electronic transitions allowed by vibronic coupling, the origin band is forbidden.

We have found the missing $\tilde{C}\,^2\Delta$ state of CaOH by direct laser excitation spectroscopy of the electronically forbidden $\tilde{C}\,^2\Delta$–$\tilde{X}\,^2\Sigma^+$ transition. We have also made the first experimental determination of the Renner–Teller parameter, $\hat{g}_4$, in a $^2\Delta$ state. To help the reader, we define our notation for the vibronic states of CaOH. We have classified the different vibrational levels in electronic states with three labels. The first of these is the electronic state, the second encloses the quanta in v_1, v_2, and v_3 with brackets (the l-type doubling quantum number appears as a superscript above v_2 when appropriate), and the last label denotes the total vibronic symmetry. Thus $\tilde{C}\,^2\Delta(010)\Phi$ denotes the $v_2 = 1$ level of the $\tilde{C}\,^2\Delta$ electronic state whose total vibronic symmetry is Φ. The reader is also referred to Fig. 1 for the relative energies of all the vibronic states arising from $v_2 = 0$, 1, and 2 in the $\tilde{C}\,^2\Delta$ and $\tilde{X}\,^2\Sigma^+$ states. It will be found useful to refer back to this figure in the subsequent sections.

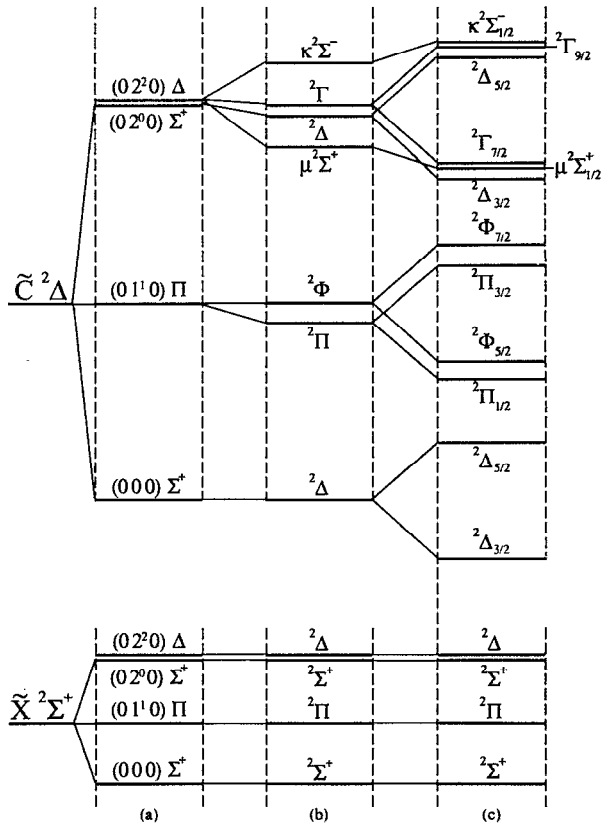

FIG. 1. The vibrational energy levels for $v=0$–2 of the $\tilde{C}\,^2\Delta$ and the $\tilde{X}\,^2\Sigma^+$ states of CaOH at different levels of theory. (a) No Renner–Teller or spin–orbit interactions considered, (b) only the Renner–Teller interaction considered, and (c) both the Renner–Teller and spin–orbit interactions included.

EXPERIMENTAL AND LOW RESOLUTION SPECTRA

CaOH and CaOD were produced in a conventional Broida oven[29] from the reaction of excited Ca atoms with H_2O and D_2O, respectively. Two lasers were used in this study, one to promote the chemical reaction by exciting a Ca atomic transition, and another to probe the molecular energy levels. The first laser was a Coherent 699 dye laser pumped by 6 W visible radiation from a Coherent Innova 70 argon ion laser and operating in linear mode with DCM dye. The bandwidth of this laser was narrowed (triple mode operation) with an etalon, and the laser was tuned to the $^3P_1$–$^1S_0$ atomic transition of Ca at 657.3 nm. The laser beam was directed into the alumina crucible containing the Ca metal in the Broida oven. The probe laser was a Coherent 699-29 ring dye laser pumped by 5 W multiline uv radiation from a Coherent Innova 200 argon ion laser and operating with Stilbene 3 dye. The laser beam was chopped with a mechanical chopper, and focused vertically into the chemiluminescent flame characteristic of CaOH production.

Initially, we scanned the probe laser broad band (1 cm^{-1} resolution), and lock-in detected the laser induced fluorescence at right angles to the beam with a photomultiplier tube. Light from the atomic pump laser was excluded by detecting through a 600 nm blue-pass filter. The spectrum for the $Ca+H_2O$ reaction displayed two major regions with many sharp bandheads degrading to the red, one starting at 450 nm and the other at 464 nm (Fig. 2). These features shifted to 451 and 462 nm (Fig. 3) when D_2O was used as oxidant, thus confirming that they were due to a molecule containing hydrogen.

Next, we fixed the probe laser on several bandheads in the 450 nm feature of CaOH, and focused the total fluorescence onto the entrance slits of a 0.64 m monochromator. The dispersed fluorescence was detected with a photomultiplier tube, processed by photon counting electronics, and recorded on chart paper. Spectra were recorded by scanning the monochromator for each laser position. The majority of the dispersed fluorescence was not resonant, and consisted of two main features at 554 and 624 nm. These features correspond to the $\tilde{B}\,^2\Sigma^+$–$\tilde{X}\,^2\Sigma^+$

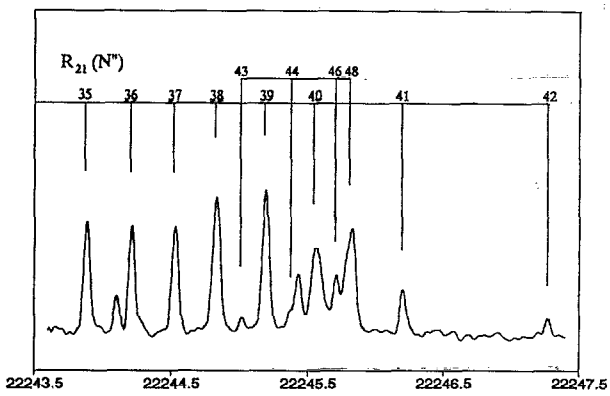

FIG. 2. The low resolution laser excitation spectrum of CaOH.

and the $\tilde{A}\,^2\Pi$–$\tilde{X}\,^2\Sigma^+$ transitions of CaOH, and confirmed that the probe laser was exciting a new electronic state of CaOH, suspected to be the $\tilde{C}\,^2\Delta$ by analogy with the isoelectronic molecule CaF.[4]

The resonant features in the dispersed fluorescence spectra were very weak, but the most intense features lay in the 464 nm region. This established that the transitions in both the 450 and the 464 nm regions connected to common upper energy levels. When the laser was placed on the highest frequency bandhead in the 450 nm region (449.7 nm), strong transitions occurred at 464.0 and 464.6 nm. The frequency differences between these resonant features and the laser position were 685(5) and 713(5) cm^{-1}, and are the same, within experimental error, as those found for the $^2\Sigma^+(02^00)\Sigma$ and $^2\Delta(02^20)\Delta$ vibrational levels in the $\tilde{X}\,^2\Sigma^+$ ground state of CaOH by Coxon *et al.*[25] [688.671(15) and 713.040(9), respectively]. Therefore, we assigned the bandhead at 449.7 nm to the $\tilde{C}\,^2\Delta(010)\Pi$–$\tilde{X}\,^2\Sigma^+(000)\Sigma$ transition, and the resonant features to the $\tilde{C}\,^2\Delta(010)\Pi$–$\tilde{X}\,^2\Sigma^+(02^00)\Sigma$ and the $\tilde{C}\,^2\Delta(010)\Pi$–$\tilde{X}\,^2\Sigma^+(02^20)\Delta$ hot bands.

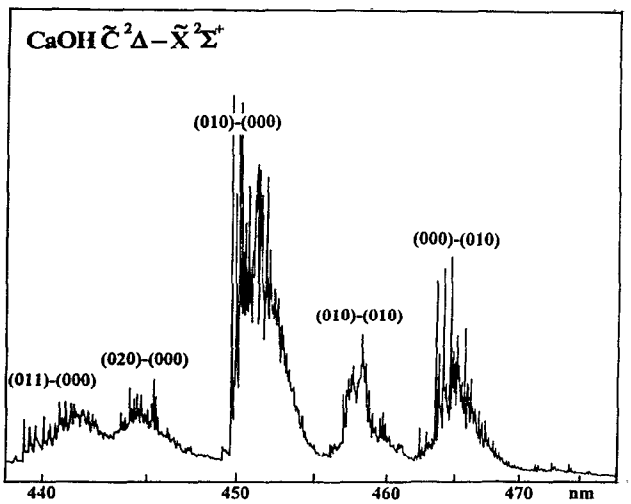

FIG. 3. The low resolution laser excitation spectrum of CaOD.

TABLE I. The positions for some of the observed bandheads for the $\tilde{C}\,^2\Delta$–$\tilde{X}\,^2\Sigma^+$ transition of CaOH.

Vibronic assignment	cm^{-1} (vac)	nm (air)
$(011)\Pi$–$(000)\Sigma$	22 751.1	439.41
$(010)\Pi$–$(000)\Sigma$	22 222.6	449.86
$(020)\Sigma$–$(010)\Pi$	22 189.6	450.53
$(011)\Pi$–$(001)\Sigma$	22 142.1	451.50
$(010)\Pi$–$(010)\Pi$	21 870.4	457.11
$(020)\Sigma$–$(02^00)\Sigma$	21 853.1	457.47
$(000)\Delta$–$(010)\Pi$	21 558.2	463.73
$(010)\Pi$–$(02^00)\Sigma$	21 533.9	464.25
$(010)\Pi$–$(02^20)\Delta$	21 509.7	464.78

Two more low resolution dye laser scans were then performed for CaOH and CaOD with a 530 nm red-pass filter also in place to prevent scattered light from the probe laser reaching the photomultiplier tube. We were, therefore, monitoring the excitation of the $\tilde{C}\,^2\Delta \leftarrow \tilde{X}\,^2\Sigma^+$ electronic transition through the emission from the $\tilde{B}\,^2\Sigma^+ \rightarrow \tilde{X}\,^2\Sigma^+$ transition. The $\tilde{B}\,^2\Sigma^+$ state was populated by collisions from the $\tilde{C}\,^2\Delta$ state. These spectra had the highest signal-to-noise ratio and are reproduced in Figs. 2 and 3 for CaOH and CaOD, respectively. In the CaOH spectrum, two strong bandheads were seen close to the positions for the $\tilde{C}\,^2\Delta(010)\Pi$–$\tilde{X}\,^2\Sigma^+(02^00)\Sigma$ and the $\tilde{C}\,^2\Delta(010)\Pi$–$\tilde{X}\,^2\Sigma^+(02^20)\Delta$ hot bands determined from the dispersed fluorescence spectra. However, more bandheads were seen at higher frequencies in the 464 nm region, and these were assigned to the $\tilde{C}\,^2\Delta(000)\Delta$–$\tilde{X}\,^2\Sigma^+(010)\Pi$ transition. It quickly became apparent that the unidentified lower frequency bandheads in the 450 nm region were hot bands in ν_2 of the $\tilde{C}\,^2\Delta(010)\Pi$–$\tilde{X}\,^2\Sigma^+(000)\Sigma$ transition. Additional vibrational features are also evident in Figs. 2 and 3, and these have been assigned as the $\tilde{C}\,^2\Delta(011)\Pi$–$\tilde{X}\,^2\Sigma^+(000)\Sigma$, the $\tilde{C}\,^2\Delta(020)\Sigma$–$\tilde{X}\,^2\Sigma^+(000)\Sigma$, and the $\tilde{C}\,^2\Delta(010)\Pi$ –$\tilde{X}\,^2\Sigma^+(010)\Pi$ vibronic bands with their associated hot bands in ν_2 running to lower frequencies.

The positions for some of the observed bandheads for CaOH are provided in Table I, from which it can be estimated that the Ca–O–H bending frequency is 312.2(10) cm^{-1} in the $\tilde{C}\,^2\Delta$ state and 352.2(10) cm^{-1} in the $\tilde{X}\,^2\Sigma^+$ state. The Ca–O stretching frequency is similarly estimated at 528.5(10) cm^{-1} in the $\tilde{C}\,^2\Delta$ state, [the value determined by Coxon *et al.*[25] in the $\tilde{X}\,^2\Sigma^+$ state was 609.015(10)]. Combining these values with the high resolution data for CaOH, enables the band origin position for the forbidden $\tilde{C}\,^2\Delta(000)\Delta$–$\tilde{X}\,^2\Sigma^+(000)\Sigma$ transition to be predicted at 21 895.7(10) cm^{-1}, 11.4 cm^{-1} lower than that for CaOD.

The bending frequencies for CaOD in the $\tilde{C}\,^2\Delta$ and in the $\tilde{X}\,^2\Sigma^+$ states are well determined in the following high resolution analysis to be 235.381(1) and 266.546(1) cm^{-1}, respectively. The Ca–O stretching frequency for the $\tilde{X}\,^2\Sigma^+$ state is measured by Coxon *et al.*[25] to be 604.903(7) cm^{-1}. However, the Ca–O stretching frequency for the $\tilde{C}\,^2\Delta$ state must be estimated from the low resolution spectra. The positions for the highest frequency bandheads

TABLE II. The fundamental vibrational frequencies for CaOH and CaOD in the $\tilde{C}\,^2\Delta$ and the $\tilde{X}\,^2\Sigma^+$ states of CaOH and CaOD.

	CaOH		CaOD	
	$\tilde{X}\,^2\Sigma^+$	$\tilde{C}\,^2\Delta$	$\tilde{X}\,^2\Sigma^+$	$\tilde{C}\,^2\Delta$
ν_1	3847(10)[a]			
ν_2	352.2(10)	312.2(10)	266.546(1)	235.381(1)
ν_3	609.015(10)[b]	528.5(10)	604.903(7)[b]	548.9(10)

[a]Reference 30.
[b]Reference 25.

in the $\tilde{C}\,^2\Delta(011)\Pi$–$\tilde{X}\,^2\Sigma^+(000)\Sigma$ and the $\tilde{C}\,^2\Delta(010)\Pi$ –$\tilde{X}\,^2\Sigma^+(000)\Sigma$ regions are 22 706.4 and 22 157.5 cm^{-1}, respectively. This allows the Ca–O stretch to be estimated at 548.9(10) cm^{-1} in the $\tilde{C}\,^2\Delta$ state.

Brazier and Bernath[30] have also measured the O–H stretching frequency of CaOH and SrOH in the $\tilde{X}\,^2\Sigma^+$ states by dispersing the fluorescence from the $\tilde{A}\,^2\Pi$ states. Their values of 3847(10) cm^{-1} for CaOH, and 3766(10) cm^{-1} for SrOH are surprisingly higher than the OH^- free-ion value of 3555.6 cm^{-1} measured by Rosenbaum *et al.*[31] The fundamental vibrational frequencies for CaOH and CaOD in the $\tilde{X}\,^2\Sigma^+$ and the $\tilde{C}\,^2\Delta$ states are summarized in Table II.

HIGH RESOLUTION SPECTRA

Following the low resolution survey scans, high resolution (1 MHz laser bandwidth) laser excitation spectra were recorded. All of the high resolution scans were performed with the 600 nm blue-pass and the 530 nm red-pass filters in place. The Doppler-limited spectra were stored as a function of frequency using Coherent's PC-Autoscan software. The frequency scale was calibrated by recording the thorium atomic lines using the optogalvanic effect at the beginning and end of each day, and comparing these frequencies with the published line list.[32] The high resolution data files were converted to ASCII format for use with the data reduction package PC-DECOMP developed at the National Solar Observatory by Brault. Each line in the high resolution spectrum was first fit to a Voigt profile using PC-DECOMP, and then the line positions and intensities were used as input to PC-LOOMIS, an interactive color Loomis–Wood[33] program written by one of the authors (Jarman) to pick out rotational branches.

At first, only the $\tilde{C}\,^2\Delta(010)\Pi$–$\tilde{X}\,^2\Sigma^+(000)\Sigma$ regions of CaOH and CaOD were recorded, because previous work had only accurately determined the rotational constants for the $\tilde{X}\,^2\Sigma^+(000)\Sigma$ level. This vibronic transition shows the same rotational structure as a Hund's case (a) $^2\Pi$–$^2\Sigma^+$ transition of a diatomic molecule with very strong Q_2 and Q_1 branches, strong R_2, R_1, P_2, and P_1 branches, and weaker Q_{21}, Q_{12}, R_{21}, P_{21}, R_{12}, and P_{12} branches. Because γ is very small for the $\tilde{X}\,^2\Sigma^+$ state of CaOH,[22] and CaOD,[23] the F_1 and F_2 components are almost coincident in energy, and so most of the satellite branches (except R_{21} and P_{12}) lie beneath stronger regular branches and have not been identified in the spectra. Thus the spectra were expected to display four distinct rotational branches

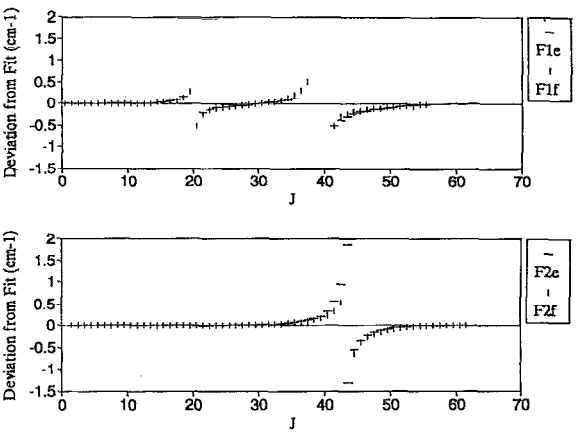

FIG. 4. A portion of the high resolution spectrum of CaOH showing the effects of the perturbation at $J'=43.5$ on the R_{21} head of the $\tilde{C}\,^2\Delta(010)\Pi$–$\tilde{X}\,^2\Sigma^+(000)\Sigma$ transition.

in two separate regions split by the spin–orbit constant A in the upper state—R_{21}, (R_2 and Q_{21}), (Q_2 and P_{21}), and P_2 in one region ($^2\Pi_{3/2}$–$^2\Sigma^+$), and R_1, (Q_1 and R_{12}), (P_1 and Q_{12}), and P_{12} in the other ($^2\Pi_{1/2}$–$^2\Sigma^+$).

The CaOH spectrum (Fig. 4) was complicated by perturbations in the upper state energy level patterns. These perturbations were evident in the Loomis–Wood plots, and allowed a definite rotational assignment to be made for the eight rotational branches. The initial fits for these branches were restricted to the low J unperturbed transitions, and were only extended to higher J values by prediction. Individual lines were fit to the N^2 Hamiltonian developed by Brown *et al.*[34] Matrix elements for this Hamiltonian are listed by Amiot *et al.*[35] for $^2\Pi$ states, and Douay *et al.*[36] for $^2\Sigma^+$ states. During this analysis we became aware of the millimeter-wave study of CaOH by Ziurys, Barclay, and Anderson,[27] and included their data in subsequent fits, effectively constraining the ground state constants to their millimeter-wave values. The final fit included transitions on both the high and low J side of the perturbations, and the resulting spectroscopic constants are displayed in Table III. The individual lines in the fit are available from PAPS,[37] or from the authors upon request.

The perturbations are portrayed as deviations from the fit graphs in Fig. 5, in which it can be seen that there are three separate perturbation regions. We are unable to offer any explanation for the weakest perturbation at $J=19.5$ in

TABLE III. The spectroscopic constants for the $\tilde{C}\,^2\Delta$ and the $\tilde{X}\,^2\Sigma^+$ states of CaOH.

	$\tilde{X}\,^2\Sigma^+(000)\Sigma$	$\tilde{C}\,^2\Delta(010)\Pi$
T	0.0	22 207.938 79(51)
A		23.040 17(86)
B	0.334 334 109 4(83)	0.322 144 7(26)
$D \times 10^{-7}$	3.859 91(22)	4.425(22)
$H \times 10^{-12}$		6.12(47)
$\gamma \times 10^{-3}$	1.159 64(13)	0.542(45)
$q \times 10^{-6}$		−3.57(99)

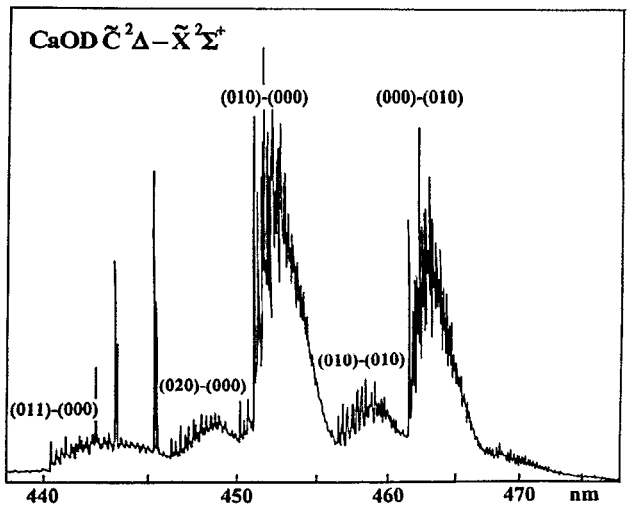

FIG. 5. The deviations from the fit for CaOH. Two perturbations are evident: one at $J'=19.5$ in the F_1 component, and the other at $J'=39.5$ and $J'=43.5$ in the F_1 and F_2 components, respectively.

the F_1 component. However, the two strongest perturbations occurring at $J=39.5$ in the F_1 component and at $J=43.5$ in the F_2 component must both be caused by the same perturbing state. This state must have a larger effective B value and start below the $\tilde{C}^2\Delta(010)\Pi$ state. The only reasonable candidate for this perturbing state is a vibration of the $\tilde{B}^2\Sigma^+$ state, whose lowest vibrational state has a 5% larger B value than the $\tilde{C}^2\Delta(010)\Pi$ state. Assuming that the perturbing state's B value is similar to that for the $\tilde{B}^2\Sigma^+(000)\Sigma$ state, the origin for the perturbing state is estimated to be 22 180 cm^{-1}, about 4160 cm^{-1} above the $\tilde{B}^2\Sigma^+(000)\Sigma$ origin. This energy difference is very close to the sum of the O–H stretching frequency and the Ca–O–H bending frequency in the $\tilde{X}^2\Sigma^+$ state, determined at 3847 and 352 cm^{-1}, respectively. Thus we hypothesize that the state responsible for the strongest perturbations is the $\tilde{B}^2\Sigma^+(110)\Pi$ state. This state would have the same vibronic symmetry as the $\tilde{C}^2\Delta(010)\Pi$ state. The large magnitude of the observed perturbations is also explained by this hypothesis: The two interacting states differ in only one quantum of an O–H stretch.

In contrast, no perturbations were evident in the CaOD spectrum, consistent with our identification of the state causing the perturbations in the CaOH spectrum as the $\tilde{B}^2\Sigma^+(110)\Pi$ state (both the Ca–O–D bend and the O–D stretch will have much lower frequencies). The eight rotational branches were easily picked out using PC-LOOMIS, and assigned by using ground state combination differences generated from the $\tilde{X}^2\Sigma^+$ constants from our previous work on the $\tilde{B}^2\Sigma^+$–$\tilde{X}^2\Sigma^+$ transition.[23] The transitions were then fit to the usual expressions for Hund's case (a) $^2\Pi$ and Hund's case (b) $^2\Sigma^+$ states, and the constants are reproduced in Table IV.

Following the analyses of the $\tilde{C}^2\Delta(010)\Pi$ –$\tilde{X}^2\Sigma^+(000)\Sigma$ bands for CaOH and CaOD, it was decided to only record more data for CaOD, because it was more likely that these bands would be unperturbed. Furthermore, the $\tilde{C}^2\Delta(000)\Delta$–$\tilde{X}^2\Sigma^+(010)\Pi$ region for CaOH lay out of the single frequency regime of our dye laser. Consequently, we took more data in the $\tilde{C}^2\Delta(010)\Pi$ –$\tilde{X}^2\Sigma^+(010)\Pi$, and the $\tilde{C}^2\Delta(000)\Delta$–$\tilde{X}^2\Sigma^+(010)\Pi$ regions of CaOD.

We initially analyzed the $\tilde{C}^2\Delta(010)\Pi$–$\tilde{X}^2\Sigma^+(010)\Pi$ region because we knew the rotational constants for the $\tilde{C}^2\Delta(010)\Pi$ state from our previous analysis and thus we could use upper state combination differences to rotationally assign the new band. This band resembled a Hund's case (a) $^2\Pi$–Hund's case (b) $^2\Pi$ transition for a diatomic molecule, and was similar in form to the $\tilde{C}^2\Delta(010)\Pi$–$\tilde{X}^2\Sigma^+(000)\Sigma$ band, except that all the lines were doubled due to the l-type doubling in the $\tilde{X}^2\Sigma^+(010)\Pi$ state. The branch intensities were also different in that all the Q branches were very weak, and many of them were only found later in the analysis by prediction. The strongest branches were the R_1, P_1, R_2, and P_2 branches. The transitions were added to those of the $\tilde{C}^2\Delta(010)\Pi$–$\tilde{X}^2\Sigma^+(000)\Sigma$ band, and the constants for all three states determined simultaneously.

TABLE IV. The spectroscopic constants for the $\tilde{C}^2\Delta$ and the $\tilde{X}^2\Sigma^+$ states of CaOD.

	$\tilde{X}^2\Sigma^+(000)\Sigma$	$\tilde{X}^2\Sigma^+(01^10)\Pi$	$\tilde{X}^2\Sigma^+(02^00)\Sigma$	$\tilde{B}^2\Sigma^+(000)\Sigma$
T	0.0	266.545 78(91)	519.189 9(11)	18 013.894 56(57)
B	0.302 954 9(66)	0.303 038 2(69)	0.303 279 8(73)	0.307 439 1(68)
$D\times10^{-7}$	2.934 (19)	3.026(27)	3.346(23)	3.071(21)
γ	0.000 953(25)	0.001 230(50)	0.001 001(67)	−0.039 586(32)
$q\times10^{-4}$		−7.631 5(54)		
	$\tilde{C}^2\Delta(000)\Sigma$	$\tilde{C}^2\Delta(010)\Pi$	$\tilde{C}^2\Delta(020)\mu\Sigma$	$\tilde{C}^2\Delta(020)\kappa\Sigma$
T	21 907.1276(11)	22 142.508 30(58)	22 368.964 0(14)	22 392.087 6(13)
A	11.494 41(55)	23.051 41(73)		
γ	−0.001 75(10)	0.001 405(34)	0.555 423(85)	0.570 104(68)
$\gamma_D\times10^{-6}$			2.311(43)	0.900(25)
B	0.293 535 9(68)	0.293 393 1(68)	0.289 455 1(94)	0.296 818 4(85)
$D\times10^{-7}$	3.282(25)	2.637(26)	−2.24(10)	7.982(61)
$H\times10^{-11}$		−0.423(35)	−8.91(39)	5.48(16)
$p\times10^{-7}$	−2.60(50)			
$q\times10^{-6}$		−3.20(50)		

We then recorded and analyzed the $\tilde{C}\,^2\Delta(000)\Delta$–$\tilde{X}\,^2\Sigma^+(010)\Pi$ transition, which was right at the red limit for the Stilbene 3 dye in our laser. This transition resembled a Hund's case (a) $^2\Delta$–Hund's case (b) $^2\Pi$ transition for a diatomic molecule, and was similar in form to the $\tilde{C}\,^2\Delta(010)\Pi$–$\tilde{X}\,^2\Sigma^+(010)\Pi$ transition, except that the Q branches were very intense. Analysis proceeded using the Loomis–Wood program to pick out rotational branches and lower state combination differences to achieve the rotational assignment. The transitions were added to those of the two other CaOD bands, and fitted together. The matrix elements for the effective $^2\Delta$ Hamiltonian used in this fit are listed in the paper by Brown, Cheung, and Merer.[38]

Thus the rotational constants for the (000) and the (010) vibrations of the $\tilde{C}\,^2\Delta$ and the $\tilde{X}\,^2\Sigma^+$ electronic states were determined simultaneously. We then predicted the positions of the $\tilde{C}\,^2\Delta(010)\Pi$–$\tilde{X}\,^2\Sigma^+(02^00)\Sigma$ and the $\tilde{C}\,^2\Delta(010)\Pi$–$\tilde{X}\,^2\Sigma^+(02^20)\Delta$ hot bands using the constants of Coxon *et al.*,[25] and we were able to identify a few rotational bands of the $\tilde{C}\,^2\Delta(010)\Pi$–$\tilde{X}\,^2\Sigma^+(02^00)\Sigma$ transition in our spectrum. The actual line positions were offset slightly from the predicted positions, and so we added these lines to our global fit and obtained a more accurate set of rotational constants for the CaOD $\tilde{X}\,^2\Sigma^+(02^00)\Sigma$ state.

THE RENNER–TELLER EFFECT

The Renner–Teller effect is the interaction of orbital angular momentum with vibrational angular momentum in linear molecules.[28,39–43] Theory incorporates this effect by describing the movement of the nuclei with two Born–Oppenheimer potentials, W_+ and W_- which touch each other at the linear configuration. The two potentials are required because the bending motion lifts the double degeneracy ($\pm\Lambda$) associated with the orbital angular momentum. The literature contains much experimental and theoretical work for linear molecules in electronic states with $\Lambda=1$ (Π states), but work on states with $\Lambda>1$ is rare. A good introduction to the theory of the Renner–Teller effect as applied to $^2\Pi$ electronic states is given by Hougen.[41] In this article, Hougen considers the effects of rotation and spin–orbit interaction explicitly, and derives formulae for the rotational energies of the Renner–Teller components.

More advanced treatments of the Renner–Teller effect are given by Brown and Jørgensen,[42,43] who consider additional anharmonic corrections to the nonrotating molecule in electronic states with $\Lambda\geqslant 1$. These authors treat the Renner–Teller effect as a perturbation to the energy levels derived from a zeroth order two dimensional degenerate harmonic oscillator Hamiltonian

$$H^0=T_{\rm nuc}+\tfrac{1}{2}\omega q^2, \tag{1}$$

where $T_{\rm nuc}$ is the kinetic energy of the nuclei and q is a dimensionless bending coordinate. The perturbing term is made up of two parts, the anharmonic terms in the average potential energy, $W-\frac{1}{2}\omega q^2$, and the term that accounts for the interaction between the W_+ and W_- potentials, $\hat{W}\sigma_Z$

$$H'=W-\tfrac{1}{2}\omega q^2+\hat{W}\sigma_Z, \tag{2}$$

where $W=\frac{1}{2}(W_+ + W_-)$ is the average potential, $\hat{W}=\frac{1}{2}(W_+ - W_-)$ is the difference potential, and σ_z is a Pauli spin matrix. Their treatment involves expanding W and $\hat{W}$ as Taylor series about the linear configuration in even powers of the bending coordinate q

$$W=W^0+W''q^2+W''''q^4+\cdots,$$
$$\hat{W}=\hat{W}''q^2+\hat{W}''''q^4+\cdots. \tag{3}$$

For an electronic Δ state, $\hat{W}''\equiv 0$, and $W''\equiv\frac{1}{2}\omega$, and so

$$H'=W''''q^4+\hat{W}''''q^4\sigma_Z=g_4q^4+\hat{g}_4q^4\sigma_Z. \tag{4}$$

Brown and Jørgensen also derive an adiabatic correction term to the potential energy, which manifests itself as an additional term $g_KJ_Z\Lambda\sigma_Y$ in H', so that the full form for the perturbing Hamiltonian (including the $AS'_Z\Lambda\sigma_Y$ spin–orbit interaction) is

$$H'=g_4q^4+\hat{g}_4q^4\sigma_Z+\{g_KJ_Z+AS'_Z\}\Lambda\sigma_Y, \tag{5}$$

where σ_Z and σ_Y are Pauli spin matrices.

Previous experimental work on the Renner–Teller effect in electronic Δ states ($\Lambda=2$), includes the work on CCN performed by Merer and Travis in 1965,[44] and the work on NCN by Kroto in 1967.[45] Merer and Travis measured the splitting (13.44 $\rm cm^{-1}$) between the Φ and the Π vibronic components arising from $v=1$ in the $\tilde{A}\,^2\Delta_i$ electronic state, and attributed it all to the second order perturbation contribution of the $\hat{g}_4q^4\sigma_Z$ term in H'. While this term does indeed contribute to the measured splitting, the $4g_K$ contribution from the adiabatic correction term, which was unknown at the time of Merer and Travis' work, is estimated to be an order of magnitude larger. Thus Merer and Travis' work on the $\tilde{A}\,^2\Delta_i$ state of CCN determined the second order parameter $g_K=3.36\ \rm cm^{-1}$, but did not determine the fourth order parameter $\hat{g}_4$.[43]

The $\hat{g}_4q^4\sigma_Z$ term in H' couples together Hund's case (a) basis functions $|\Lambda l\rangle$ differing in both Λ and l by 4 and in $K=\Lambda+l$ by 0, and so it only affects the energies of Renner–Teller components arising from $v\geqslant 2$, because only these can have l differing by 4. For $v=2$, this term couples $|2,-2\rangle$ with $|-2,2\rangle$, and so couples together two $K=0$ Renner–Teller components that are degenerate in the absence of spin–orbit coupling. These components are labeled $\mu\Sigma$ and $\kappa\Sigma$, where $\mu\Sigma$ refers to the lower energy component, and $\kappa\Sigma$ the higher. From the work of Brown and Jørgensen, it can be deduced that the 2×2 matrix that needs to be diagonalized to obtain correct first order energies for the $\mu\Sigma$ and $\kappa\Sigma$ states is

$$\begin{matrix}|2,-2\rangle\\|-2,2\rangle\end{matrix}\begin{pmatrix}A & 12\hat{g}_4\\ 12\hat{g}_4 & -A\end{pmatrix}. \tag{6}$$

This matrix is similar in form to that connecting the two $K=0$ Renner–Teller components for $v=1$ in a $^2\Pi$ state (see Hougen[41]). Consequently, we can apply the results of

Hougen's rotational perturbation calculations to the two $K=0$ components for $v=2$ in the $\tilde{C}\,^2\Delta$ state of CaOD, and hence obtain a value for $\hat{g}_4$. In the present case, $A \gg BJ$, and so Hougen's work predicts that the $\mu\Sigma$ and $\kappa\Sigma$ states will look more like two case (a) $^2\Pi_{1/2}$ components rather than $^2\Sigma^+$ and $^2\Sigma^-$ components. Although these states have Σ vibronic symmetry, they arise from a $^2\Delta$ electronic state with substantial spin–orbit splitting. The reader is referred to the paper by Kopp and Hougen[46] for more information on Hund's case (a) $^2\Sigma$ states, including a useful diagram showing the J correlations between case (a) and case (b) $^2\Sigma$ states.

Having already obtained rotational constants for the $\tilde{X}\,^2\Sigma^+(010)\Pi$ vibronic state of CaOD, we therefore searched for the $\tilde{C}\,^2\Delta(020)\mu\Sigma$–$\tilde{X}\,^2\Sigma^+(010)\Pi$ and $\tilde{C}\,^2\Delta(020)\kappa\Sigma$–$\tilde{X}\,^2\Sigma^+(010)\Pi$ hot bands in the (010)–(000) region of the spectrum. These bands were expected to look like case (a) $^2\Pi_{1/2}$–case (b) $^2\Pi$ transitions, similar in form to the lower frequency component of the $\tilde{C}\,^2\Delta(010)\Pi$–$\tilde{X}\,^2\Sigma^+(010)\Pi$ band, but with stronger Q branches. However, as can be seen in Fig. 1, the $^2\Delta_{5/2}$ and the $^2\Delta_{3/2}$ spin components are also predicted to lie close to the $\kappa\Sigma$ and $\mu\Sigma$ components, and transitions to these components from the $\tilde{X}\,^2\Sigma^+(010)\Pi$ vibronic state are both symmetry allowed and expected to display similar rotational structure. Consequently, we needed an independent check to verify that we were seeing transitions to the $\kappa\Sigma$ and $\mu\Sigma$ components, and not to the $^2\Delta_{5/2}$ and the $^2\Delta_{3/2}$ spin components.

This check came from finding the $\tilde{C}\,^2\Delta(020)$ $\mu\Sigma$–$\tilde{X}\,^2\Sigma^+(020)\Sigma$ and the $\tilde{C}\,^2\Delta(020)\kappa\Sigma$–$\tilde{X}\,^2\Sigma^+(020)\Sigma$ hot bands in the (010)–(010) region of the spectrum. The vibronic assignment for the (020)–(020) hot band was made definite because the difference between the highest frequency bandheads in the observed (020)–(010) and the (020)–(020) hot bands matched the difference between the $\tilde{X}\,^2\Sigma^+(02^00)\Sigma$ and the $\tilde{X}\,^2\Sigma^+(01^10)\Pi$ term values found by Coxon *et al.*,[25] but did not match the difference between the $\tilde{X}\,^2\Sigma^+(02^20)\Delta$ and the $\tilde{X}\,^2\Sigma^+(01^10)\Pi$ states. Thus the observed transitions were connecting to vibronic states within the $\tilde{C}\,^2\Delta$ electronic state which had Σ symmetry—the $(020)\mu\Sigma$ and $(020)\kappa\Sigma$ Renner–Teller components.

The rotational analysis of the $\tilde{C}\,^2\Delta(020)$ $\mu\Sigma$–$\tilde{X}\,^2\Sigma^+(010)\Pi$ and the $\tilde{C}\,^2\Delta(020)\kappa\Sigma$–$\tilde{X}\,^2\Sigma^+(010)\Pi$ hot bands proceeded smoothly using the Loomis–Wood program and lower state combination differences generated from our previous fits to the $\tilde{X}\,^2\Sigma^+(010)\Pi$ state. We also assigned the $\tilde{C}\,^2\Delta(020)\mu\Sigma$–$\tilde{X}\,^2\Sigma^+(020)\Sigma$ and the $\tilde{C}\,^2\Delta(020)\kappa\Sigma$–$\tilde{X}\,^2\Sigma^+(020)\Sigma$ hot bands in our high resolution spectrum, but excluded the lines in our fits because of a 0.04 cm^{-1} calibration error in our spectrum. We initially fitted the $\tilde{C}\,^2\Delta(020)\mu\Sigma$–$\tilde{X}\,^2\Sigma^+(010)\Pi$ and the $\tilde{C}\,^2\Delta(020)\kappa\Sigma$–$\tilde{X}\,^2\Sigma^+(010)\Pi$ transitions varying only the spectroscopic parameters for the $\mu\Sigma$ and the $\kappa\Sigma$ vibronic states. Then we performed a final combined fit of all the observed data for CaOD, and the values for the parameters obtained from this fit are the values reported in Table IV.

In Table IV, it can be seen that the effective value for the spin–rotation constant γ is very close to twice the value for the B constant for both the $\mu\Sigma$ and the $\kappa\Sigma$ states. This is because both states are very close to Hund's case (a) limit, for which γ would be $2B$. The effective values found from the fit are related to their real physical counterparts[38] as follows:

$$B^{\kappa}_{\text{eff}}=B[1+(B/2r)\cos^2 2\beta], \tag{7}$$

$$D^{\kappa}_{\text{eff}}=D[1+(2B/r)\cos^2 2\beta], \tag{8}$$

$$\gamma^{\kappa}_{\text{eff}}=2B[1-|\sin 2\beta|+(B/2r)\cos^2 2\beta], \tag{9}$$

$$\gamma^{\kappa}_{D\ \text{eff}}=2D[1-|\sin 2\beta|+(2B/r)\cos^2 2\beta], \tag{10}$$

and

$$B^{\mu}_{\text{eff}}=B[1-(B/2r)\cos^2 2\beta]; \tag{11}$$

$$D^{\mu}_{\text{eff}}=D[1-(2B/r)\cos^2 2\beta], \tag{12}$$

$$\gamma^{\mu}_{\text{eff}}=2B[1-|\sin 2\beta|-(B/2r)\cos^2 2\beta], \tag{13}$$

$$\gamma^{\mu}_{D\,\text{eff}}=2D[1-|\sin 2\beta|-(2B/r)\cos^2 2\beta], \tag{14}$$

where $r\sin 2\beta = 12\hat{g}_4$, $r\cos 2\beta=A$, and $\{2r + (\gamma^{\kappa} - \gamma^{\mu})/2\}$ is the difference between the $\mu\Sigma$ and the $\kappa\Sigma$ band origins.

Taking values from Table IV, one obtains $r = 11.5581(10)$ cm^{-1} from the band-origin positions and the values for γ in the $\mu\Sigma$ and $\kappa\Sigma$ states. Averaging the values for the $\mu\Sigma$ and $\kappa\Sigma$ states gives $B=0.293\,136\,8(63)$ cm^{-1}, and $D = 2.876(60) \times 10^{-7}$ cm^{-1}. From the average of the γ values, and the value for B, one obtains $|\sin 2\beta| = 0.040\,101(94)$ cm^{-1}, giving $|\hat{g}_4| = 0.038\,624(91)$ cm^{-1}. As a test of the internal consistency of the above equations [Eqs. (7)–(14)] these parameter values predict $B^{\kappa}_{\text{eff}}=0.296\,848$ cm^{-1}, $D^{\kappa}_{\text{eff}} = 3.02\times10^{-7}$ cm^{-1}, $\gamma^{\kappa}_{\text{eff}}=0.570\,19$ cm^{-1}, and $\gamma^{\kappa}_{D\,\text{eff}} = 5.81\times10^{-7}$ cm^{-1}, as well as $B^{\mu}_{\text{eff}}=0.289\,426$ cm^{-1}, $D^{\mu}_{\text{eff}}=2.73\times10^{-7}$ cm^{-1}, $\gamma^{\mu}_{\text{eff}}=0.555\,34$ cm^{-1}, and $\gamma^{\mu}_{D\,\text{eff}}=5.23\times10^{-7}$ cm^{-1}. The agreement with the observed parameters for the main constants B and γ is excellent, but [Eqs. (7)–(14)] provide only semiquantitative results for D and γ_D. In addition, these constants predict $A_{\Delta} = 11.5488$ cm^{-1} for $v=2$, and this obeys the general trend of increasing values for A_{Δ} with increasing v [$A_{\Delta} = A_{\Pi}/2 = 11.5257(4)$ cm^{-1} for $v=1$, and $A_{\Delta} = 11.4944(6)$ cm^{-1} for $v=0$].

The Eqs. (7)–(14) are only sensitive to the magnitude of $\hat{g}_4$, some additional information is needed to determine its sign. The isovalent CaSH molecule is bent, and Ortiz has calculated the position of the electronic states by *ab initio* techniques.[47] He finds that the $\tilde{C}\,^2\Delta$ state of linear CaSH correlates to the $\tilde{D}\,^2A'$, and the $\tilde{E}\,^2A''$ states in the bent configuration. Since the A'' state is associated with the W_- potential surface, and the A' state with the W_+ potential, the work of Ortiz implies that $\hat{g}_4$ is negative for CaSH [$\hat{W} = (W_+ - W_-)/2$ and $\sigma_{\text{reflection}}(W_{\pm}) = \pm(W_{\pm})$]. Assuming that CaSH and CaOH are similar, then $\hat{g}_4$ is expected to be negative in the $\tilde{C}\,^2\Delta$ state of CaOH. This is found to be the case experimentally because

the upper $\kappa\Sigma$ state behaves like a $^2\Sigma^-$ state, and the lower $\mu\Sigma$ state like a $^2\Sigma^+$ state. This can only happen if the W_- curve lies above the W_+ curve and $\hat{g}_4$ is negative.

CONCLUSIONS

We have measured the forbidden electronic transitions $\tilde{C}\,^2\Delta$–$\tilde{X}\,^2\Sigma^+$ of CaOH and CaOD, made possible by exploiting the Herzberg–Teller interaction with the bending mode. The energy pattern for the vibrational levels in the $\tilde{C}\,^2\Delta$ state are determined by the Renner–Teller effect. We have measured this effect for $v=2$ in the $\tilde{C}\,^2\Delta$ state of CaOD, and determined the first experimental value for the difference in the quartic potential constants, $\hat{g}_4 = -0.038\,624(91)$ cm^{-1}. In addition, we have determined the molecular spin–orbit one-electron parameter $a_\delta = 2A$, for the $\tilde{C}\,^2\Delta(000)\Delta$ state of CaOD at about 23 cm^{-1}, which is almost identical to the free ion value for the $3d$ atomic orbital of Ca^+ ($\zeta=24$ cm^{-1}). Therefore, we conclude that the $\tilde{C}\,^2\Delta$ state of CaOH and CaOD is made up almost entirely of the $3d$ atomic orbital of Ca^+, and that the bonding in CaOH is nearly 100% ionic.

ACKNOWLEDGMENTS

We thank J. Coxon for providing a copy of Ref. 25 in advance of publication. This work was supported by the National Science Foundation (CHE-8913785) and the Centres of Excellence in Molecular and Interfacial Dynamics.

[1] T. Törring, W. E. Ernst, and J. Kändler, J. Chem. Phys. **90**, 4927 (1989).
[2] P. F. Bernath, Science **254**, 665 (1991).
[3] S. F. Rice, H. Martin, and R. W. Field, J. Chem. Phys. **82**, 5023 (1985).
[4] P. F. Bernath, Ph.D. dissertation, Massachusetts Institute of Technology, 1980.
[5] E. S. Rittner, J. Chem. Phys. **19**, 1030 (1951).
[6] J. V. Ortiz, J. Chem. Phys. **92**, 6728 (1990).
[7] P. Bündgen, B. Engels, and S. D. Peyerimhoff, Chem. Phys. Lett. **176**, 407 (1991).
[8] J. D'Incan, C. Effantin, A. Bernard, J. Vergès, and R. F. Barrow, J. Phys. B **24**, L71 (1991).
[9] C. W. Bauschlicher, Jr. and H. Partridge, Chem. Phys. Lett. **106**, 65 (1984).
[10] C. W. Bauschlicher, Jr., S. R. Langhoff, and H. Partridge, J. Chem. Phys. **84**, 901 (1986).
[11] C. W. Bauschlicher, Jr., S. R. Langhoff, T. C. Steimle, and J. E. Shirley, J. Chem. Phys. **93**, 4179 (1990).
[12] J. M. Mestdagh and J. P. Visticot, Chem. Phys. **155**, 79 (1991).
[13] R. F. Barrow, B. J. Howard, A. Bernard, and C. Effantin, Mol. Phys. **72**, 971 (1991).
[14] A. Bernard, C. Effantin, J. d'Incan, G. Fabre, R. Stringat, and R. F. Barrow, Mol. Phys. **67**, 1 (1989).
[15] C. Effantin, A. Bernard, J. d'Incan, G. Wannous, J. Vergès, and R. F. Barrow, Mol. Phys. **70**, 735 (1990).
[16] A. Bernard, C. Effantin, J. d'Incan, J. Vergès, and R. F. Barrow, Mol. Phys. **70**, 747 (1990).
[17] C. Amiot and J. Vergès, Chem. Phys. Lett. **185**, 310 (1991).
[18] H. Martin and P. Royen, Chem. Phys. Lett. **97**, 127 (1983).
[19] W. T. M. L. Fernando, M. Douay, and P. F. Bernath, J. Mol. Spectrosc. **144**, 344 (1990).
[20] R. C. Hilborn, Z. Qingshi, and D. O. Harris, J. Mol. Spectrosc. **97**, 73 (1983).
[21] P. F. Bernath and S. Kinsey-Nielsen, Chem. Phys. Lett. **105**, 663 (1984).
[22] P. F. Bernath and C. R. Brazier, Astrophys. J. **288**, 373 (1985).
[23] R. A. Hailey, C. N. Jarman, W. T. M. L. Fernando, and P. F. Bernath, J. Mol. Spectrosc. **147**, 40 (1991).
[24] J. A. Coxon, M. Li, and P. I. Presunka, J. Mol. Spectrosc. **150**, 33 (1991).
[25] J. A. Coxon, M. Li, and P. I. Presunka, Mol. Phys. (submitted).
[26] T. C. Steimle, D. A. Fletcher, K. Y. Jung, and C. T. Scurlock, J. Chem. Phys. **96**, 2556 (1992).
[27] L. M. Ziurys, W. L. Barclay, and M. A. Anderson, Astrophys. J. **384**, L63 (1992).
[28] G. Herzberg, *Electronic Spectra and Electronic Structure of Polyatomic Molecules* (Krieger, Malabar, FL., 1991).
[29] J. B. West, R. S. Bradford, J. D. Eversole, and C. R. Jones, Rev. Sci. Instrum. **46**, 164 (1975).
[30] C. R. Brazier and P. F. Bernath (unpublished results).
[31] N. H. Rosenbaum, J. C. Owrutsky, L. M. Tack, and R. J. Saykally, J. Chem. Phys. **84**, 5308 (1986).
[32] B. A. Palmer and R. Engleman, Jr., *Atlas of the Thorium Spectrum* (Los Alamos National Labs, Los Alamos, 1983), p. 9615.
[33] F. W. Loomis and R. W. Wood, Phys. Rev. **32**, 223 (1928).
[34] J. M. Brown, E. A. Colbourn, J. K. G. Watson, and F. D. Wayne, J. Mol. Spectrosc. **74**, 294 (1979).
[35] C. Amiot, J. P. Maillard, and J. Chauville, J. Mol. Spectrosc. **87**, 196 (1981).
[36] M. Douay, S. A. Rogers, and P. F. Bernath, Mol. Phys. **64**, 425 (1988).
[37] See AIP document no. PAPS JCPSA-97-1711-10 for 10 pages of tables. Order by PAPS number and journal reference from American Institute of Physics, Physics Auxiliary Publication Service, 335 East 45th Street, New York, NY 10017. The price is $1.50 for each microfiche (60 pages) or $5.00 for photocopies of up to 30 pages, and $0.15 for each additional page over 30 pages. Airmail additional. Make checks payable to the American Institute of Physics.
[38] J. M. Brown, A. S-C. Cheung, and A. J. Merer, J. Mol. Spectrosc. **124**, 464 (1987).
[39] G. Duxbury, Mol. Spectrosc. Chem. Soc. Specialist Periodical Rep. **3**, 497 (1975).
[40] A. J. Merer and C. Jungen, *Molecular Spectroscopy: Modern Research*, Vol. II, edited by K. N. Rao (Academic, New York, 1976).
[41] J. T. Hougen, J. Chem. Phys. **36**, 519 (1962).
[42] J. M. Brown and F. Jørgensen, Mol. Phys. **47**, 1065 (1982).
[43] J. M. Brown and F. Jørgensen, *Advances in Chemical Physics*, Vol. 52, edited by I. Prigogine and S. A. Rice (Wiley, New York, 1983).
[44] A. J. Merer and D. N. Travis, Can. J. Phys. **43**, 1795 (1965).
[45] H. W. Kroto, Can. J. Phys. **45**, 1439 (1967).
[46] I. Kopp and J. T. Hougen, Can. J. Phys. **45**, 2581 (1967).
[47] J. V. Ortiz, Chem. Phys. Lett. **169**, 116 (1990).